

Two-dimensional material nanophotonics

Fengnian Xia^{1*}, Han Wang², Di Xiao³, Madan Dubey⁴ and Ashwin Ramasubramaniam⁵

Two-dimensional materials exhibit diverse electronic properties, ranging from insulating hexagonal boron nitride and semiconducting transition metal dichalcogenides such as molybdenum disulphide, to semimetallic graphene. In this Review, we first discuss the optical properties and applications of various two-dimensional materials, and then cover two different approaches for enhancing their interactions with light: through their integration with external photonic structures, and through intrinsic polaritonic resonances. Finally, we present a narrow-bandgap layered material — black phosphorus — that serendipitously bridges the energy gap between the zero-bandgap graphene and the relatively large-bandgap transition metal dichalcogenides. The plethora of two-dimensional materials and their heterostructures, together with the array of available approaches for enhancing the light-matter interaction, offers the promise of scientific discoveries and nanophotonics technologies across a wide range of the electromagnetic spectrum.

Many-layered materials in their bulk forms have been widely known and utilized for a long time. For example, graphite and MoS₂ are used as dry lubricants owing to their layered nature, whereby atoms are strongly bonded within the same plane but only weakly attached to sheets above and below by van der Waals forces. This weak interlayer interaction makes the extraction of single or a few layers of atoms possible, thus leading to the burgeoning research on two-dimensional (2D) materials^{1–15}, including their photonic properties and applications. In this Review, we broadly define 2D materials to include multilayers, heterostructures and layered thin films whose total thicknesses vary from one atomic layer to tens of nanometres. 2D here implies that the thickness of the material under investigation is orders of magnitude smaller than the wavelength of light involved.

Compared with traditional 3D photonic materials such as gallium arsenide (GaAs) and silicon (Si), 2D materials exhibit many exceptional properties. First, quantum confinement in the direction perpendicular to the 2D plane leads to novel electronic and optical properties that are distinctively different from their bulk parental materials^{2,3,11,12}. Second, their surfaces are naturally passivated without any dangling bonds, which makes it easy to integrate 2D materials with photonic structures such as waveguides^{16–19} and cavities^{20–24}. It is also possible to construct vertical heterostructures²⁵ using different 2D materials without the conventional ‘lattice mismatch’ issue, as layers with different lattice constants in heterostructures are only weakly bonded by van der Waals force as in layered bulk materials. Third, despite being atomically thin, many 2D materials interact strongly with light. For example, a single layer of MoS₂ absorbs around 10% of vertically incident light at excitonic resonances (615 nm and 660 nm)²⁶. Finally, 2D materials can cover a very wide range of the electromagnetic spectrum because of their diverse electronic properties (Fig. 1a).

Graphene, being gapless and semimetallic, interacts with light from microwave to ultraviolet wavelengths^{27,28}, thus making it a potential candidate for various light detection, modulation and manipulation applications over a wide spectral range. However, its semimetallic nature prevents the realization of efficient graphene-based light-emitting devices. In contrast, single-layer transition metal dichalcogenides (TMDCs) such as molybdenum disulfide (MoS₂) and tungsten diselenide (WSe₂) are direct-bandgap semiconductors^{11,12} (Fig. 1c) that exhibit encouraging light-emitting properties primarily

in the near-infrared wavelength range. Here, emission is dominated by excitons and trions due to the strong Coulomb interactions arising from their low dimensionality and reduced dielectric screening. Furthermore, as will be discussed later, the breaking of inversion symmetry and strong spin-orbit coupling in TMDCs lead to valley-selective circular dichroism^{15,29–32}. Different valleys can be pumped selectively using left- and right-circularly polarized light to generate carriers with different magnetic moments, leading to the emerging field known as valleytronics. Hexagonal boron nitride (hBN) is another important type of 2D material¹⁰. It has a large bandgap of around 6 eV (Fig. 1b), which makes it an excellent dielectric, and can be incorporated into various heterostructures for the electrostatic gating of other 2D materials, as the ‘lattice match’ is not necessary in these van der Waals heterostructures. Other than graphene, TMDCs and hBN, the recently rediscovered black phosphorus (BP) exhibits a direct bandgap of around 0.3 eV in its bulk form³³. The bandgap of BP is expected to increase monotonically as the number of layers decreases, owing to electronic confinement in the direction perpendicular to the 2D plane, and single layer BP is estimated to reach a single-particle bandgap of around 2 eV (Fig. 1d)³⁴. The wide range of material properties, together with the possibilities for combining 2D materials with different layer numbers and compositions, allows for the realization of various nanophotonic devices and the exploration of fundamental optical sciences, covering a wide spectral range from the microwave to the ultraviolet (Fig. 1a).

Photonic devices using 2D materials

The unique optical properties of 2D materials enable many important device applications in nanophotonics.

Photodetection mechanisms in graphene. Graphene attracts significant attention for photodetection because of its strong interaction with photons in a wide energy range^{27,28} and its high carrier mobility, making it a promising candidate for high-speed light detection applications in a broad wavelength range. In early studies, the photodetection mechanism in graphene was attributed to the traditional photovoltaic effect^{35–37} as in 3D semiconductors such as GaAs and Si, whereby photocurrent results from the separation of photogenerated electron–hole pairs by a built-in electric field.

However, subsequent investigations by Xu *et al.*³⁸ revealed a more complex situation, owing to the gapless nature and reduced

¹Department of Electrical Engineering, Yale University, 15 Prospect Street, New Haven, Connecticut 06511, USA. ²Ming Hsieh Department of Electrical Engineering, University of Southern California, 3737 Watt Way, Los Angeles, California 90089, USA. ³Department of Physics, Carnegie Mellon University, 5000 Forbes Avenue, Pittsburgh, Pennsylvania 15213, USA. ⁴Army Research Laboratory, Sensors and Electron Devices Directorate, 2800 Power Mill Road, Adelphi, Maryland 20783, USA. ⁵Department of Mechanical and Industrial Engineering, University of Massachusetts, Amherst, 160 Governors Drive, Amherst, Massachusetts 01003, USA. *e-mail: fengnian.xia@yale.edu

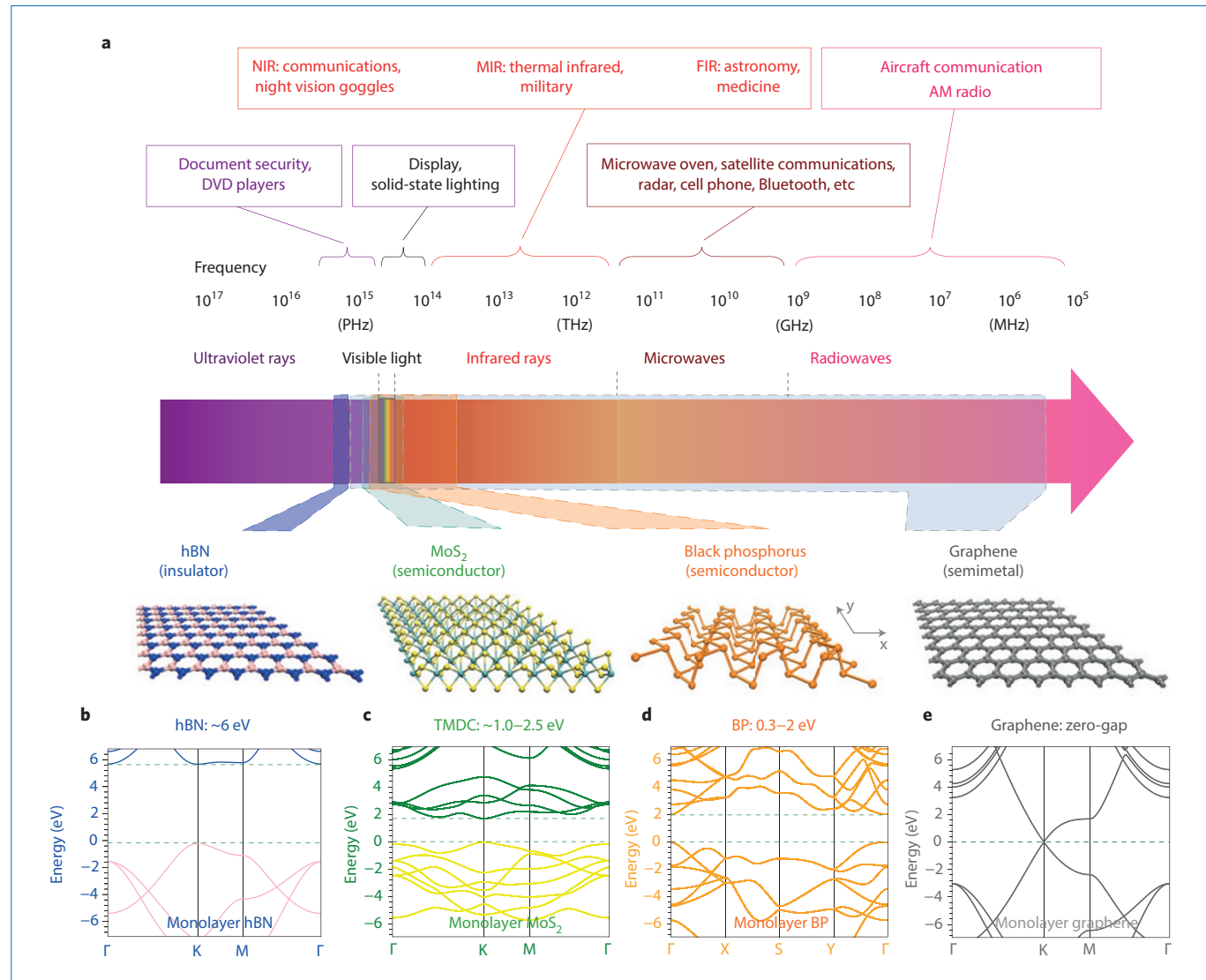


Figure 1 | 2D materials covering a broad spectral range. **a**, Electromagnetic spectrum. Applications that utilize the different spectral ranges are presented in the top portion of the panel. NIR, MIR and FIR indicate near-, mid- and far-infrared, respectively. The atomic structures of hBN, MoS₂, BP and graphene are shown in the bottom of the panel, left to right. The crystalline directions (x and y) of anisotropic BP are indicated. The possible spectral ranges covered by different materials are indicated using coloured polygons. **b–e**, Bandstructures of single-layer hBN (**b**), MoS₂ (**c**), BP (**d**) and graphene (**e**).

dimensionality of graphene. First, the acoustic phonon decay bottleneck and low heat capacity of single- and few-layer graphene mean that the electronic temperature T_E can be significantly higher than the lattice temperature T_L under optical excitation^{39,40}. If the doping of graphene under illumination is uniform, there is no net photocurrent generated due to the T_E gradient as the carriers will diffuse in all possible directions from the centre to the edge within the illumination spot. However, if there is doping nonuniformity in graphene, for example in a graphene p–n junction, a net photocurrent driven by these ‘hot’ carriers — a phenomenon called the photo-thermoelectric (PTE) effect³⁸ — can be observed. Second, owing to the zero-bandgap nature of graphene, carrier–carrier scattering quickly (on a subpicosecond timescale) thermalizes photo-excited electrons and holes in the conduction and valence bands through Auger-type processes, thus leading to a common quasi-Fermi level for both types of carriers^{41–43}. At the same time, the Auger-type impact ionization due to strong carrier–carrier interaction can also generate multiple electron–hole pairs with a single photon — an effect called carrier multiplication^{44,45}. Carrier multiplication in graphene occurs even

under zero external bias. This is fundamentally different from the multiplication effect in traditional avalanche photodetectors, in which carriers are first accelerated under a high electric field to provide them with enough energy to excite additional electrons from the valence band to the conduction band. In short, the carrier dynamics in graphene under illumination are different in many respects from those in 3D semiconductors with a significant bandgap, where photocarriers have longer lifetimes and are usually generated by photons with energies similar to the semiconductor bandgap. As a result, the photogenerated electrons and holes in traditional semiconductors are characterized by well-separated quasi-Fermi levels and the carrier temperature usually does not significantly differ from the lattice temperature.

Gabor *et al.*⁴⁶ demonstrated that at a dual-gated graphene p–n junction (Fig. 2a), the photovoltage exhibits a six-fold polarity variation pattern when the top and bottom gate biases change (Fig. 2b) — a signature of the PTE effect. The changing of photocurrent polarity for multiple times is attributed to the non-monotonic dependence of the graphene Seebeck coefficient on gate biases, which governs

the photovoltage (or current) due to the PTE effect. On the contrary, if the traditional photovoltaic effect dominates, the polarity of the photocurrent only depends on the direction of the built-in electric field, and thus multiple polarity variations as a function of gate biases are not expected.

Freitag *et al.*⁴⁷ explored photocurrents in biased graphene. Figure 2c denotes a reflection image of a graphene field-effect transistor under investigation with a channel measuring $1\text{ }\mu\text{m} \times 6\text{ }\mu\text{m}$. A constant source-drain bias of 1 V is applied to the device and the photocurrent is determined by comparing the source-drain current with and without light illumination. In this case, three photocurrent generation mechanisms are identified: the traditional photovoltaic effect, the PTE effect, and the bolometric effect. As shown in Fig. 2d, when the channel doping is high (but uniform), the PTE effect is negligible, as discussed above. The photovoltaic effect does exist but the bolometric effect is dominant: the total current decreases under light excitation as the increase in temperature causes a reduction in carrier mobility. When the graphene channel is intrinsic (Fig. 2e, gate bias V_G close to Dirac point voltage V_{Dirac}), the traditional photovoltaic effect dominates because the increase in carrier temperature leads to extra electrons and holes⁴⁸, thus enhancing the total current. In intrinsic graphene, the carrier mobility is much less sensitive to temperature⁴⁹ and so the bolometric effect can be ignored. Furthermore, although in this case a finite drain bias V_D will introduce a slightly non-uniform doping along the graphene channel, the PTE effect will reduce the total current under light illumination (Fig. 2e) and, from the polarity of the photocurrent, it is clear that the photovoltaic effect dominates in this case. Figure 2f summarizes the polarity of the photocurrent under different biasing conditions.

It has been shown experimentally by many groups that graphene photodetectors can operate at speeds greater than tens of gigahertz^{7,17–20}. Photocurrents arising from the photovoltaic effect are intrinsically suitable for such high-speed operation (up to hundreds of gigahertz) owing to the high carrier mobility and high carrier saturation velocity. For the PTE effect, the maximum speed of operation depends on the carrier cooling time, which can be longer than 100 ps⁴⁶. This relatively long carrier cooling time in graphene can still support photodetector operation in the gigahertz range. However, enhancement of photocurrent due to the PTE effect requires the suppression of cooling channels to increase the carrier temperature T_E , which inevitably leads to a longer cooling time and thus lower speed. Effective utilization of multiple photocurrent generation mechanisms in graphene for different optical applications is an important future research topic. In addition, the carrier multiplication effect may be leveraged to further enhance the performance of graphene photodetectors.

Light-emitting properties and circular dichroism in TMDCs. Unlike graphene, some members of the TMDC family are true semiconductors with appreciable bandgaps. In particular, molybdenum- and tungsten-based dichalcogenides exhibit optical bandgaps in the range of 1–2 eV, which makes them suitable for near-infrared absorption and emission. Interestingly, although these materials have an indirect bandgap in the bulk and few-layer form, they become direct-gap semiconductors with strong photoluminescence at the monolayer level^{11,12}. Bandgaps in TMDCs have also been shown to be tunable — over a range from semiconducting to near-metallic — through application of an external electric field or mechanical strain^{50–52}, which is a useful property for engineering the optoelectronic response for specific applications. Duerloo *et al.* showed theoretically that mechanical deformations can switch thermodynamic stability between a semiconducting and a metallic crystal structure in Mo- and W-dichalcogenide monolayers⁵³. They further identified that molybdenum telluride (MoTe_2) can be an excellent candidate for the observation of such phase transitions, which can be utilized to manipulate the optical response of the materials.

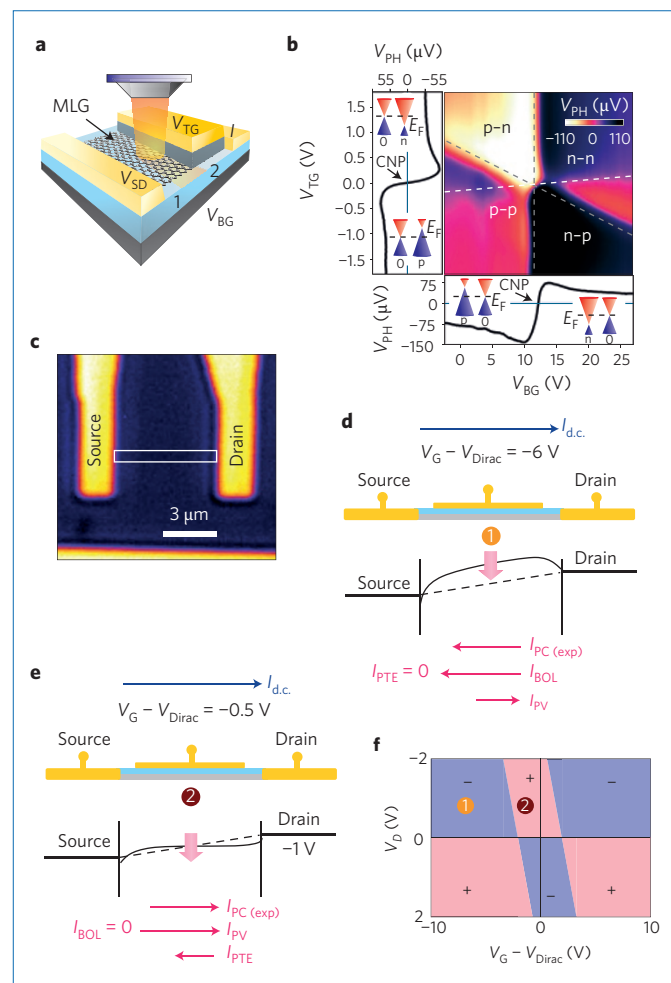


Figure 2 | Photocurrent-generation mechanisms in graphene. **a**, Schematic of a dual-gated graphene field-effect transistor for photocurrent generation. **b**, Six-fold photovoltage pattern that occurs when the top and bottom gate biases change. The incident light spot is focused on the junction interface. Left and bottom panels show photovoltage patterns taken along the vertical and diagonal lines, respectively. **c**, A reflection image of the graphene field-effect transistor for a biased photocurrent experiment. **d**, Energy diagram and photocurrent-generation mechanism for a strongly doped channel. The total photocurrent I_{PC} is opposite to the d.c. current $I_{\text{d.c.}}$, which indicates that the dominant component is the bolometric photocurrent I_{BOL} . **e**, Energy diagram and photocurrent-generation mechanism for an intrinsic graphene channel. The total photocurrent I_{PC} is dominated by the traditional photovoltaic component I_{PV} . **f**, Total photocurrent polarity for conditions (**d**) and (**e**), indicated by 1 and 2, respectively. Here, + denotes a photocurrent flowing from source to drain and - indicates the opposite. Figure reproduced with permission from: **a,b**, ref. 46, © 2011 AAAS; **c-f**, ref. 47, Nature Publishing Group.

More importantly, TMDC monolayers have been shown to display unique physics hitherto unobserved in other 2D materials. In contrast with conventional semiconductors such as GaAs, the direct bandgap in TMDC monolayers occurs at the two unequalled corners (K and K') of the hexagonal Brillouin zone, thereby endowing the electrons with a valley degree of freedom¹⁵. It was predicted that the lack of an inversion centre in the crystal structure leads to valley-contrasting orbital magnetic moment and circular dichroism²⁹, which allows selective pumping of valley carriers by controlling the circular polarization of light^{30–32}. It is also possible, vice versa, to make polarized LEDs in TMDC monolayer p–n junctions^{54–56} (Fig. 3a). In

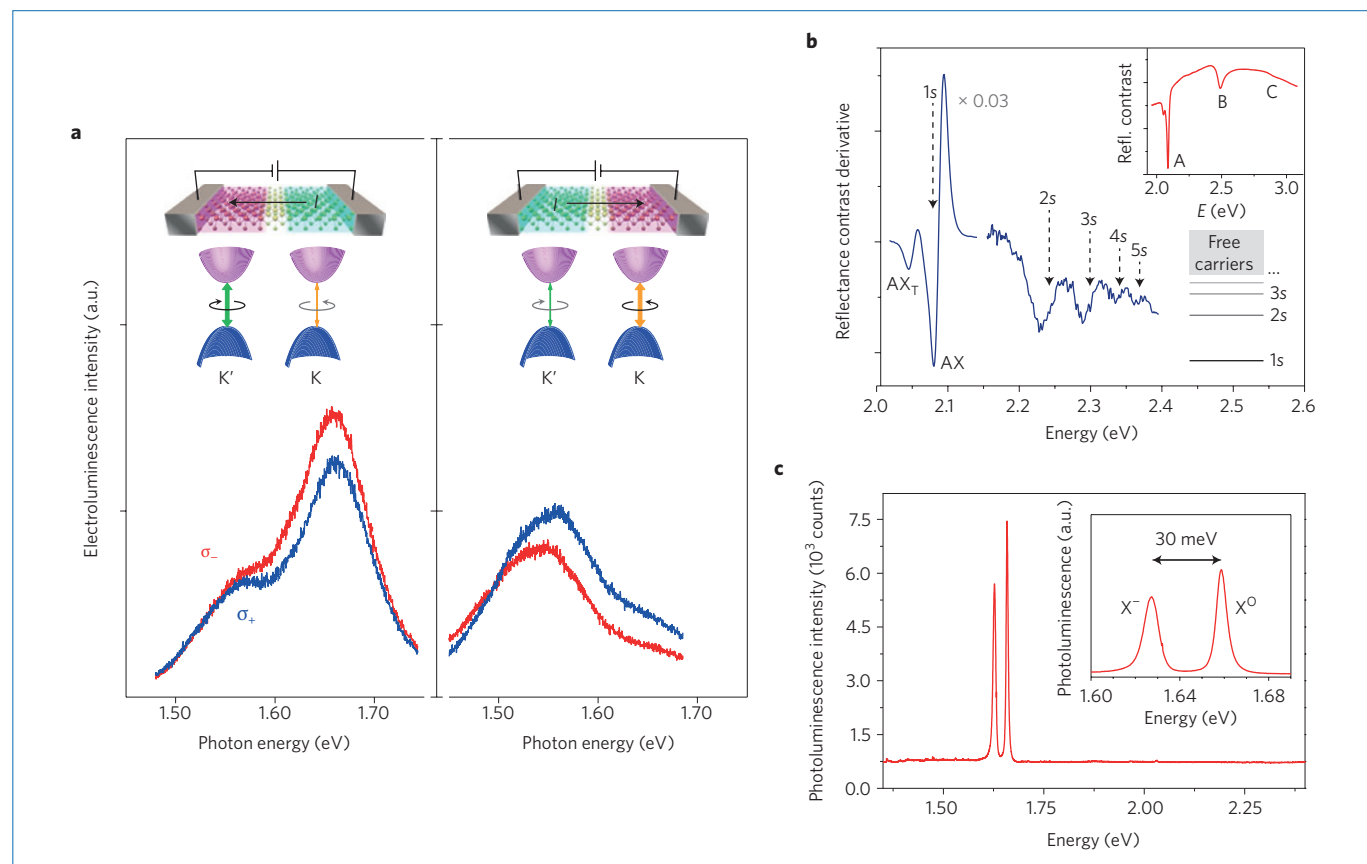


Figure 3 | Optoelectronic properties of semiconducting TMDC monolayers. **a**, Polarization-resolved electroluminescence spectra from a WSe_2 p-i-n junction. Left and right panels show the spectra dominated by σ_- and σ_+ circularly polarized light, respectively. Also shown are the current-flowing directions and the K and K' valleys. **b**, Derivative of the reflection contrast spectrum for a WS_2 monolayer. Excitonic Rydberg series (A-type excitons) are labelled using the quantum orbital terminology of 1s, 2s and so on. AX and AX_T denote 1s exciton and trion transitions, respectively. Inset: reflection contrast spectrum. Main transition peaks correspond to A, B and C excitons. **c**, Photoluminescence spectrum of monolayer $MoSe_2$ at 20 K. Inset: detailed view showing both exciton (X^0) and trion (X^-) peaks. The binding energy of X^- is 30 meV. Figure reproduced with permission from: **a**, ref. 54, © 2014 AAAS; **b**, ref. 60, © 2014 APS; **c**, ref. 62, Nature Publishing Group.

this case, the electric field at the junction preferably populates the carriers in one particular valley (K or K'), depending on the field direction. As a result, reversing the field direction switches the dominant polarization (σ_+ or σ_-) in the emitted light⁵⁴. Such TMDC monolayer p-n junctions can also be used for light detection and energy harvesting⁵⁷. Additionally, excitonic valley coherence has also been demonstrated⁵⁸. This type of dynamic control of valley index opens up the exciting possibility of valleytronics — optoelectronic devices and systems based on the manipulation of the electrons' valley index. Furthermore, the strong spin-orbit coupling arising from transition metals locks the valley index with the electron spin, which could be useful for many optoelectronic applications. For example, the injection of carriers with specific spins through ferromagnetic contacts can create a population imbalance between the two valleys, thereby potentially providing LEDs with a dominant polarization state (σ_+ or σ_-).

Another important property of TMDC monolayers is their large exciton binding energy (0.5–1 eV) arising from the substantially reduced dielectric screening relative to the bulk^{59,60}. This leads to strong and long-lived excitons, thus making such devices suitable for LEDs, photomarkers and other related applications. Figure 3b shows the Rydberg excitonic series in a reflection contrast spectrum of monolayer WS_2 . Finally, the strong Coulomb interaction also allows the observation of trions — quasiparticles comprised of two electrons and a hole (or two holes and an electron) — in doped

monolayer TMDCs under optical excitation^{61,62}. Figure 3c shows the photoluminescence spectrum of a monolayer $MoSe_2$ at 20 K. Both exciton (X^0) and trion (X^-) peaks are observed. From the energy spacing between X^0 and X^- , a trion bonding energy of 30 meV is determined. These quasiparticles, which are unstable in conventional semiconductors due to the screened Coulomb interaction, have binding energies an order of magnitude larger than that of GaAs quantum wells and display valley-selective properties that are similar to those of the neutral excitons. However, unlike excitons, trions, being charged quasiparticles, are amenable to manipulation by electric fields, which could allow for the exploration of charge transport by composite particles⁶³ and the efficient collection of photo-generated current, rather than relying on carrier diffusion alone.

Light harvesting and detection using 2D heterostructures. Despite being atomically thin, the surface of a 2D material is self-passivated without any dangling bonds. As a result, it is possible to construct functional devices by combining different 2D materials with very different lattice constants to form heterostructures, thereby leveraging the desirable properties of each material. Britnell *et al.*⁶⁴ sandwiched a thin layer of WS_2 within two layers of graphene to form an efficient ‘Schottky-diode-like’ solar cell. In this device, the semiconducting WS_2 functions as the active energy-harvesting material, whereas the metallic graphene works as a transparent electrode for the efficient collection of photogenerated carriers. Researchers demonstrated an

extrinsic quantum efficiency of 30% in the visible spectral range using just 50 nm of WS₂, which highlights the great potential of TMDCs in solar energy harvesting. Although previously both MoS₂ and WS₂ have been explored for photovoltaic applications⁶⁵, the reintroduction of TMDCs in the novel 2D heterostructure form allows for the greatly improved photocarrier extraction efficiency. Photocarriers only need to travel less than tens of nanometres before being collected, thus providing a viable approach for the utilization of TMDCs in realistic photovoltaic applications. Yu *et al.*⁶⁶ reported a photodetector based on a graphene–MoS₂–graphene heterostructure, for which they achieved an external quantum efficiency of more than 50% at a wavelength of 500 nm. In both heterostructures, because a single layer of graphene cannot screen the electric field effectively, the photoresponse can be tuned using a back gate underneath the bottom graphene contact, which offers flexibility in electrical tuning. Future research on the wafer-scale production of such graphene/TMDC vertical heterostructures may lead to practical ultrathin solar cells.

It is also possible to realize photocurrent gain by integrating graphene with other photodetection materials. Konstantatos *et al.*⁶⁷ integrated lead sulfide (PbS) quantum dots with a graphene transistor to produce a phototransistor with a photoconductive gain of more than 2×10^8 . In this device, efficient light absorption is due to the PbS quantum dots; the long carrier lifetime in PbS allows the photocarriers to reach a high density, which effectively modifies the graphene channel doping. This, together with graphene's high mobility, allows a large gain to be achieved. Similar high-gain photodetection is also observed in graphene–TMDC heterostructures⁶⁸. In these devices, large gain usually implies a slower device response. As a result, it is essential to optimize the gain and response time simultaneously for different applications.

Enhancing the interaction using photonic integration

Many 2D materials interact strongly with light. Both graphene and single-layer MoS₂ have absorption coefficients of more than $5 \times 10^7 \text{ m}^{-1}$ in the visible range (if normalized to the corresponding atomic thickness)²⁶ — this is an order of magnitude larger than the absorption coefficients of GaAs and Si. However, owing to the innate thinness of graphene and single-layer MoS₂, such a strong interaction must be further enhanced before it can be used in practical devices. The integration of 2D materials with external photonic structures offers a solution in this respect. In particular, integration with optical cavities allows for the significant manipulation of the local optical density of states surrounding the 2D materials, thus leading to greatly modified emission/absorption properties.

The integration of ultrathin optical materials with an optical waveguide is a classic approach for enhancing the light–matter interaction in a non-resonant manner. Liu *et al.*¹⁶ integrated wafer-scale monolayer graphene with a Si optical waveguide to produce a broadband optical modulator covering the telecommunications range of 1.3–1.6 μm (Fig. 4a). Because a single layer of graphene absorbs around 2% of vertically incident light through inter-band transitions in the near-infrared, it is only possible to modulate the transmission from 98% to 100% if graphene is used directly for light-modulation purposes. By propagating the light in the silicon optical waveguide beneath the graphene (Fig. 4a), the light absorption is no longer limited to 2% but is rather determined by the length of the waveguide. Using a 100- μm -long silicon waveguide, Liu *et al.*¹⁶ demonstrated a graphene modulator operating at a bandwidth of more than 1 GHz and a modulation depth of 10 dB. A similar concept was used independently by three groups to enhance the responsivity of graphene high-speed photodetectors for optical communications (Fig. 4b–d)^{17–19}. A maximum responsivity of around 0.15 A W⁻¹ and a 3 dB bandwidth of around 20 GHz were realized in a broad wavelength range from 1.3 to 1.6 μm , enabled by the non-resonant nature of the silicon optical waveguide. However, a relatively long

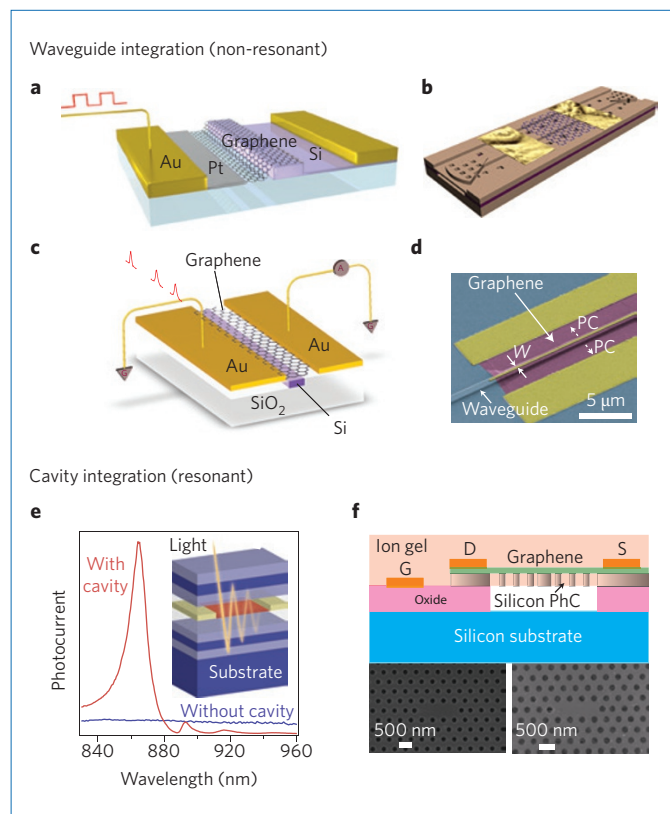


Figure 4 | Using photonic integration to enhance the interaction between light and 2D materials. **a**, Schematic of a high-bandwidth graphene modulator integrated with a silicon waveguide. **b**, Schematic of graphene/silicon heterojunctions used for light detection. **c**, A slightly different integration scheme for a graphene photodetector and a silicon waveguide. In this case, graphene functions as the detection material, whereas the silicon waveguide confines and guides the light. **d**, Scanning electron micrograph of a graphene photodetector integrated with a silicon waveguide (false colour). **e**, Photocurrent spectra measured from graphene photodetectors inside (red) and outside (blue) a Fabry-Pérot cavity. Inset: schematic of the graphene detector inside the cavity. **f**, Top: schematic of an electrically tunable graphene device integrated with a silicon nanocavity. Bottom: scanning electron micrographs showing the silicon cavity before (left) and after (right) graphene deposition. Figure reproduced with permission from: **a**, ref. 16, Nature Publishing Group; **b**, ref. 18, Nature Publishing Group; **c**, ref. 17, Nature Publishing Group; **d**, ref. 19, Nature Publishing Group; **e**, ref. 20, © 2012 ACS; **f**, ref. 22, © 2013 ACS.

waveguide length (tens to hundreds of micrometres) is needed to achieve high absorption in graphene, which makes the total device much longer than the operational wavelength. Because the area of the metallic contacts scales proportionally with device length, these waveguide-integrated graphene devices have a relatively large capacitance, which limits the operational bandwidth to tens of gigahertz.

In contrast, the integration of 2D materials with an optical cavity makes the realization of compact devices possible at the expense of a reduced light–matter interaction bandwidth, which is determined by the quality factor of the cavity. Furchi *et al.*²⁰ achieved a 26-fold enhancement in graphene's absorption by integrating a graphene photodetector with a microcavity consisting of Bragg mirrors on both sides (Fig. 4e). The limited enhancement is attributable to the relatively low quality factor of the microcavity, as the Bragg mirrors provide optical confinement only in the vertical direction. Instead, the integration of graphene with a high quality factor, silicon photonic

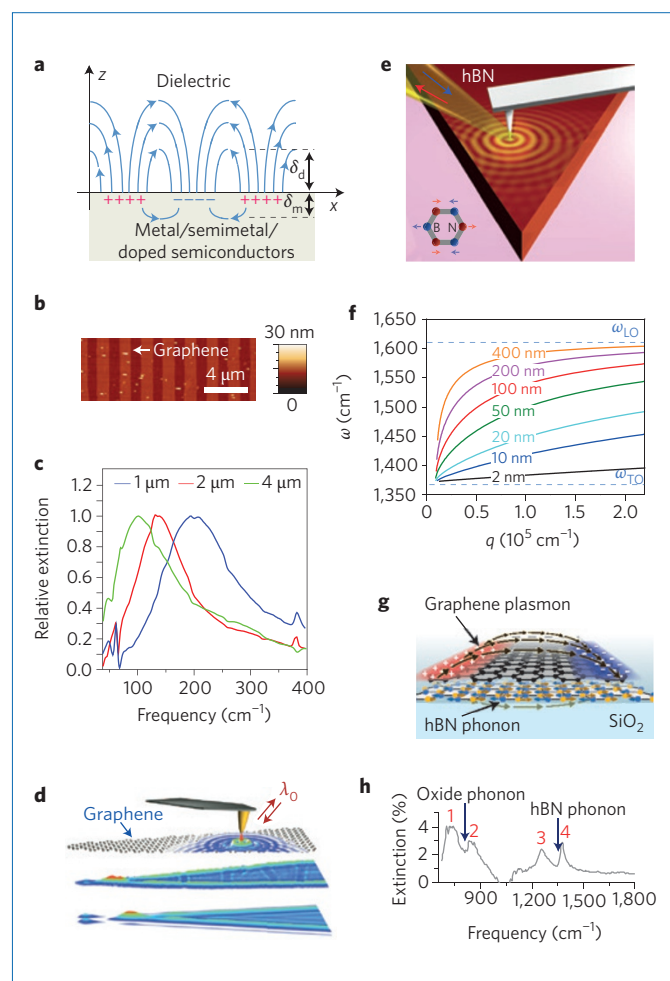


Figure 5 | Using polaritonic resonances to enhance the interaction between light and 2D materials. **a**, Plasmon-polariton wave at the metal-dielectric interface. The field can be tightly confined at the interface owing to the negative permittivity of metal. The field decaying length in both dielectric (δ_d) and metal (δ_m) can be much smaller than the wavelength of the light. **b**, Atomic force micrographs of an array of graphene nanoribbons, in which localized plasmons can be excited using vertical incident light with polarization perpendicular to the ribbons. **c**, Relative extinction spectra due to localized plasmon resonance in ribbons with widths of 1 μm , 2 μm and 4 μm , respectively. **d**, Top: experimental schematic for launching plasmon-polariton waves using a scanning near-field optical microscopy tip in a graphene wedge. The tip is illuminated using infrared light and collection of the local field in graphene is also realized using the tip. Middle: measured local field in graphene. Bottom: calculated local field in graphene. Standing waves are formed due to reflections at the edges. $\lambda_0 = 9.7 \mu\text{m}$. **e**, Experimental schematic for launching phonon-polariton waves using a scanning near-field optical microscopy tip in an hBN wedge. Inset: schematic showing the relative motions of the boron and nitride atoms. ω_{LO} and ω_{TO} are longitudinal and transverse optical phonon frequencies in bulk hBN, respectively. **f**, Calculated phonon-polariton dispersion relations at different hBN thicknesses. **g**, A schematic diagram showing the coupling between the graphene plasmon and the hBN phonon. **h**, Transmission extinction spectrum for an array of graphene nanoribbons (300 nm wide) on a single layer of hBN on an SiO_2 substrate. Peaks 1 and 2 are due to the coupling of graphene plasmons and SiO_2 phonons, whereas peaks 3 and 4 result from the coupling of graphene plasmons and hBN phonons. Figure reproduced with permission from: **b,c**, ref. 76, Nature Publishing Group; **d**, ref. 80, Nature Publishing Group; **e,f**, ref. 83, © 2014 AAAS; **g**, ref. 85, © 2014 ACS.

crystal (PhC) cavity allows for a much greater enhancement²² because confinement exists in all three dimensions; through in-plane Bragg reflections from periodic holes, and total internal reflection in the out-of-plane direction. Figure 4f shows such an integration scheme (top), together with the silicon cavity before (bottom-left) and after (bottom-right) graphene deposition. This scheme could potentially be utilized to realize graphene modulators and detectors with ultra-compact footprint and ultrahigh modulation speed. However, the operation wavelength range will be limited by the cavity resonance bandwidth. Furthermore, the integration of cavities with single-layer TMDCs allows the emission properties to be modified, which may ultimately lead to TMDC-based nanolasers^{23,24}.

Enhancing the interaction using polaritonic resonances

Another approach for enhancing the interaction of light and 2D materials is to use their intrinsic polaritonic resonances. Polaritons are quasiparticles that result from the coupling of photons with electric dipole-carrying elementary excitations such as plasmons, phonons and excitons. The wide variety of 2D materials makes the exploration of different polaritonic excitations possible.

Plasmon–polaritons in graphene. Propagating plasmon–polariton waves in a metal–dielectric interface are often used to confine the light beyond the traditional diffraction limit by leveraging the negative permittivity of metal (Fig. 5a)⁶⁹. Because the dispersion relation (frequency ω against momentum k) of light in free space is well above that of the plasmon–polariton wave, excitation of the propagating plasmon–polariton wave requires special k -matching techniques to satisfy the boundary condition at the interface⁶⁹. Besides propagating plasmon–polariton waves, highly confined, localized plasmon modes also exist in micro- and nanostructures. In both cases, confinement beyond the diffraction limit leads to a highly concentrated light field at the corresponding interface, and thus to an enhanced light–matter interaction. Direct excitation of the localized plasmon modes is possible because in micro- and nanostructures translational symmetry is lost and thus momentum conservation is no longer needed. Metallic graphene can support both propagating and localized plasmons^{70–75}.

Ju *et al.*⁷⁶ patterned a large piece of monolayer graphene into microribbons (Fig. 5b) and observed terahertz localized plasmon resonances when the incident light polarization was perpendicular to the ribbons, as the ribbons can only be effectively polarized for plasmon excitation along the perpendicular direction. Figure 5c shows the extinction spectra for ribbons with widths of 1 μm , 2 μm and 4 μm , which together indicate the size dependence of plasmon resonance in a 2D electron gas. The plasmon resonance peak and amplitude can be tuned using a gate bias, which demonstrates the unique *in situ* tunability of graphene plasmons. For graphene micro- and nanodisks, localized plasmons can be excited regardless of the light polarization due to the high structural symmetry. Furthermore, utilization of multiple graphene layers effectively enhances the strength of the plasmon resonance through dipole–dipole coupling among layers, and infrared filters and polarizers have been demonstrated using such graphene stacks⁷⁷. Finally, the relativistic mass in graphene has been revealed in the exploration of plasmon resonances^{76,77}.

Another innovative approach for exciting plasmons in graphene is to use a scanning near-field optical microscopy tip (Fig. 5d, top)^{78–80}. In this configuration, the nanoscale metallic tip is illuminated with infrared light and the additional momentum required for the excitation of graphene plasmon–polaritons is provided by the tip. The tip is also used to probe the plasmon–polariton waves in graphene. The bottom two panels in Fig. 5d represent the measured and calculated light intensities, respectively, at a plasmonic resonance of 9.7 μm . Standing-wave patterns are observed due to reflections at the graphene edges.

Compared with plasmons in metals, graphene plasmons cover a relatively less-explored wavelength range of the terahertz to the mid-infrared^{81,82}. The unique electrical tunability of plasmons in graphene makes it possible to realize optical modulators in this wavelength range. Together with the PTE effect discussed above, graphene plasmonic resonance may also be utilized to construct high-performance tunable photodetectors covering this broad wavelength range. Furthermore, improvements in graphene quality may ultimately lead to plasmon–polariton waveguides that exhibit high confinement beyond the diffraction limit, with propagation lengths exceeding tens of polariton wavelengths. Another important research task is to extend the graphene plasmon resonance to the near-infrared by suppressing the damping pathway through the emission of its intrinsic optical phonon⁸¹.

Phonon–polaritons and plasmon–phonon–polaritons. Similar to traditional polar substrates such as silicon oxide, 2D hexagonal boron nitride (hBN) supports phonon–polaritons, quasiparticles that result from the coupling of photons and dipole-carrying optical phonons. Dai *et al.* investigated phonon–polaritons at the hBN surface by employing the same scanning near-field optical microscopy technique used to probe plasmon–polaritons (Fig. 5e)⁸³. The layered nature of hBN makes it possible to tune the phonon–polariton resonance in a layer-by-layer manner. Figure 5f shows the calculated dispersion relationships of phonon–polaritons at different hBN thicknesses. The phonon–polariton resonance range accessed by varying the hBN thickness may allow for the realization of tunable mid-infrared optoelectronic devices.

By placing the graphene on polar substrates such as SiO₂ or BN, plasmons in graphene and phonons in polar substrates can couple if their energies and momenta match, leading to a new mixed state known as plasmon–phonon–polaritons^{84,85}. Figure 5g illustrates such a coupling process and Fig. 5h shows an extinction spectrum for a graphene–hBN ribbon array on an SiO₂ substrate, with a graphene ribbon width of around 300 nm. The presence of multiple extinction peaks is due to the coupling of graphene plasmon, SiO₂ surface polar phonon and hBN phonon modes. Exploring the coupling between plasmons and phonons will not only provide useful information on the interactions of carriers and substrates, but may also further enable light detection and modulation functions, leveraging the unique properties of both plasmons and phonons.

Bridging the bandgap using layered black phosphorus

Researchers have extensively explored zero-gap graphene and semiconducting single-layer TMDCs such as MoS₂ and WSe₂, which have optical bandgaps greater than 1 eV. Recently rediscovered layered-material black phosphorus, which has high mobility (up to 50,000 cm² V⁻¹ s⁻¹ in bulk at 30 K) and a direct bandgap of around 0.3 eV, bridges the gap between the gapless graphene and large-bandgap TMDCs³³, thereby making it an interesting addition to the existing 2D material family for nanophotonics and nanoelectronics^{86–91}. Based on thin-film (more than ten layers) BP, transistors with field-effect mobility from a few hundred to 1,000 cm² V⁻¹ s⁻¹ and photodetectors operational at 1.5 μm have recently been demonstrated^{86–90}. Furthermore, by reducing the number of layers, the bandgap of BP is expected to increase monotonically to around 2 eV (single-particle bandgap) in the monolayer form, thereby covering a broad energy range.

The most striking property of layered BP is probably its in-plane anisotropy. Xia *et al.* measured the infrared extinction spectra of thin-film (around 30 nm) BP at different incident light polarizations (Fig. 6a)⁸⁹. Compared with graphene, puckered BP exhibits lower symmetry (Fig. 1a), which results in in-plane anisotropic properties in momentum space^{33,34,89,92}. The bandstructure of BP is more dispersive in the *x*-direction (armchair), which leads to higher carrier mobility

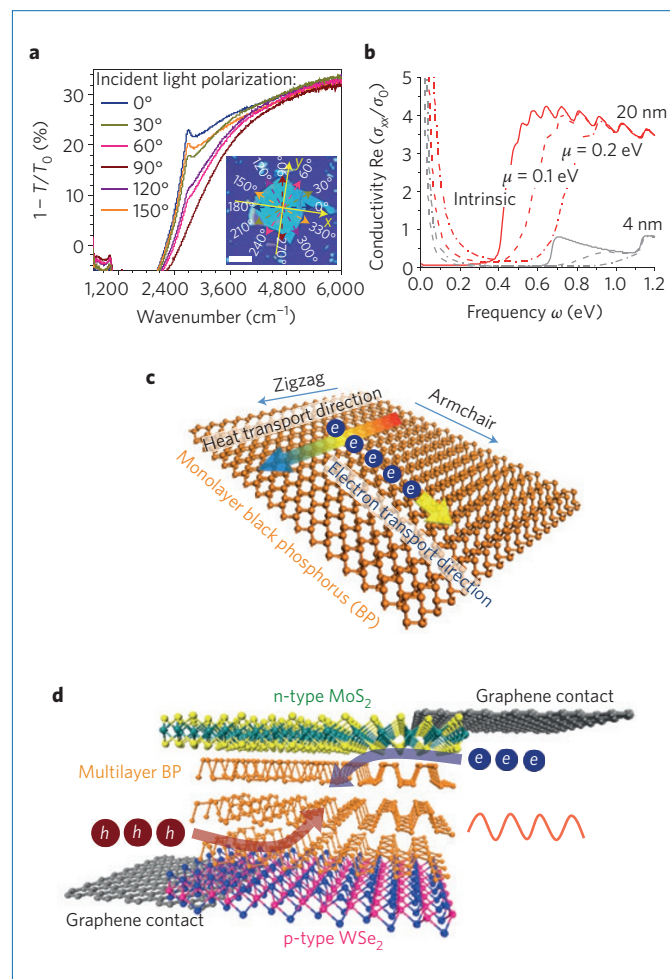


Figure 6 | Bridging the bandgap using BP. **a**, Polarization-resolved infrared extinction spectra of thin-film BP with a thickness of around 30 nm. Inset: optical image of the BP thin film. The light polarizations used in measurements are shown in the inset image. The scale bar is 20 μm. The direction of 0° is chosen randomly in the measurement; in this case it is around 8° off the *x*-axis of the BP crystal. **b**, Calculated dynamical conductivities along the *x*-direction of BP thin films at different doping levels. The Fermi-level in BP is denoted by μ . Red lines: BP thickness of 20 nm; grey lines: BP thickness of 4 nm. **c**, Orthogonality between the dominant heat and electron transport directions in single-layer BP. The figure is inspired by a similar drawing in ref. 95. **d**, Schematic of an LED that uses 2D heterostructures. A thin film of narrow-bandgap BP is sandwiched between large-bandgap TMDCs with *p*- and *n*-doping for the injection of holes and electrons, respectively. Figure reproduced with permission from: **a**, ref. 89, Nature Publishing Group; **b**, ref. 93, © 2014 APS.

and greater optical conductivity along this direction⁹². Figure 6b plots the calculated thin-film BP conductivity along the *x*-direction at different doping levels for BP thicknesses of 4 nm and 20 nm, which reveals the great potential of BP for infrared (1–5 μm) modulation functions⁹³, in addition to its promising future for light detection⁸⁸. The phononic properties of BP are also highly anisotropic, and the Raman scattering spectra of thin-film BP strongly depends on the polarization of the excitation light⁸⁹. In addition to the traditional mid- and near-infrared emission, modulation and detection devices, its unique anisotropic electronic, photonic and phononic properties may allow for the realization of novel optical components such as polarization sensors and anisotropic plasmonic devices⁹⁴. More interestingly, the preferable electron and heat conduction pathways in monolayer BP

are along the armchair and zigzag directions, respectively, which are orthogonal to each other (Fig. 6c). This unique property makes monolayer BP a promising material for thermoelectric applications with a high thermoelectric figure of merit⁹⁵.

It is also possible to construct photonic devices using heterostructures comprising both narrow-bandgap BP and larger-bandgap TMDCs. Figure 6d denotes such an infrared LED. Here, the direct-bandgap BP, whose bandgap can be tuned by varying the layer number (0.3 eV being the minimum), is utilized as an active material for light emission. The injection of holes and electrons can be realized by using p-type WSe₂ and n-type MoS₂, respectively. The injected carriers are trapped within BP for light emission due to the band-offset at the BP-TMDC interface. Graphene can be used to minimize the contact resistance⁹⁶. Lasing might also be possible if such an LED were to be integrated with a high-quality optical cavity. Phototransistors with gain and electro-absorption modulators in the mid- and near-infrared spectral range can also be built based on this concept of vertical van der Waals heterostructures.

Outlook

The emerging field of 2D materials provides the optical community with many exciting new opportunities for exploration of sciences and technologies across a very wide electromagnetic spectral range. Gapless graphene strongly interacts with light from the terahertz to the ultraviolet. Plasmon-polaritons in graphene allow for a highly confined light field and a greatly enhanced light-matter interaction at resonance. Coupling of plasmons in graphene and phonons in a polar dielectric forms a new type of quasi-particle: plasmon-phonon-polaritons, which can be utilized to enhance and tune the interaction between light and 2D materials. Although graphene is not an optimal material for light emission, many single-layer TMDCs are direct-bandgap semiconductors and exhibit strong excitonic emission properties that are gate-tunable, which makes them promising candidates for light emission in the near-infrared. Furthermore, the breaking of inversion-symmetry accompanied by strong spin-orbit coupling in such single layers results in the unique ‘valley polarization’, which has spawned the emerging field of valleytronics.

The bandgap of BP, a recently rediscovered layered material, is around 0.3 eV in its bulk form and is expected to increase monotonically as the layer number decreases to around 2 eV in its monolayer form, thus bridging the energy gap between gapless graphene and large-bandgap TMDCs. Furthermore, it may be possible to incorporate arsenic (As) into BP, leading to layered As_xP_{1-x} with a bandgap possibly below 0.3 eV (ref. 97). The wide variety of available 2D materials, together with the approaches discussed here (through integration with external photonic structures and through intrinsic polaritonic resonances) for enhancing the light-matter interaction, may enable the discovery of new optical sciences and the realization of various light emission, detection, modulation and manipulation applications.

Received 22 July 2014; accepted 6 October 2014; published online 27 November 2014

References

- Novoselov, K. S. *et al.* Electric field effect in atomically thin carbon films. *Science* **306**, 666–669 (2004).
- Novoselov, K. S. *et al.* Two-dimensional gas of massless Dirac fermions in graphene. *Nature* **438**, 197–200 (2005).
- Zhang, Y., Tan, Y. W., Stormer, H. L. & Kim, P. Experimental observation of the quantum Hall effect and Berry’s phase in graphene. *Nature* **438**, 201–204 (2005).
- Nair, R. R. *et al.* Fine structure constant defines visual transparency of graphene. *Science* **320**, 1308 (2008).
- Mak, K. F. *et al.* Measurement of the optical conductivity of graphene. *Phys. Rev. Lett.* **101**, 196405 (2008).
- Wang, F. *et al.* Gate-variable optical transitions in graphene. *Science* **320**, 206–209 (2008).
- Xia, F., Mueller, T., Lin, Y.-M., Valdes-Garcia, A. & Avouris, P. Ultrafast graphene photodetector. *Nature Nanotech.* **4**, 839–843 (2009).
- Bao, Q. *et al.* Broadband graphene polarizer. *Nature Photon.* **5**, 411–415 (2011).
- Bonaccorso, F., Sun, Z., Hasan, T. & Ferrari, A. C. Graphene photonics and optoelectronics. *Nature Photon.* **4**, 611–622 (2010).
- Dean, C. R. *et al.* Boron nitride substrates for high-quality graphene electronics. *Nature Nanotech.* **5**, 722–726 (2010).
- Mak, K. F. *et al.* Atomically thin MoS₂: A new direct-gap semiconductor. *Phys. Rev. Lett.* **105**, 136805 (2010).
- Splendiani, A. *et al.* Emerging photoluminescence in monolayer MoS₂. *Nano Lett.* **10**, 1271–1275 (2010).
- Grigorenko, A. N., Polini, M. & Novoselov, K. S. Graphene plasmonics. *Nature Photon.* **6**, 749–758 (2012).
- Chhowalla, M. *et al.* The chemistry of two-dimensional layered transition metal dichalcogenide nanosheets. *Nature Chem.* **5**, 263–275 (2013).
- Xu, X., Yao, W., Xiao, D. & Heinz, T. F. Spin and pseudospins in layered transition metal dichalcogenides. *Nature Phys.* **10**, 343–350 (2014).
- Liu, M. *et al.* A graphene-based broadband optical modulator. *Nature* **474**, 64–67 (2011).
- Gan, X. *et al.* Chip-integrated ultrafast graphene photodetector with high responsivity. *Nature Photon.* **7**, 883–887 (2013).
- Wang, X., Cheng, Z., Xu, K., Tsang, H. K. & Xu, J. High-responsivity graphene/silicon-heterostructure waveguide photodetectors. *Nature Photon.* **7**, 888–891 (2013).
- Pospischil, A. *et al.* CMOS-compatible graphene photodetector covering all optical communication bands. *Nature Photon.* **7**, 892–896 (2013).
- Furchi, M. *et al.* Microcavity-integrated graphene photodetector. *Nano Lett.* **12**, 2773–2777 (2012).
- Gan, X. *et al.* Strong enhancement of light-matter interaction in graphene coupled to a photonic crystal nanocavity. *Nano Lett.* **12**, 5626–5631 (2012).
- Majumdar, A., Kim, J., Vuckovic, J. & Wang, F. Electrical control of silicon photonic crystal cavity by graphene. *Nano Lett.* **13**, 515–518 (2013).
- Gan, X. *et al.* Controlling the spontaneous emission rate of monolayer MoS₂ in a photonic crystal nanocavity. *Appl. Phys. Lett.* **103**, 181119 (2013).
- Sobhani, A. *et al.* Enhancing the photocurrent and photoluminescence of single crystal monolayer MoS₂ with resonant plasmonic nanoshells. *Appl. Phys. Lett.* **104**, 031112 (2014).
- Geim, A. K. & Grigorieva, I. V. Van der Waals heterostructures. *Nature* **499**, 419–425 (2014).
- Eda, G. & Maier, S. A. Two-dimensional crystals: Managing light for optoelectronics. *ACS Nano* **7**, 5660–5665 (2013).
- Mak, K. F., Ju, L., Wang, F. & Heinz, T. F. Optical spectroscopy of graphene: From the far infrared to the ultraviolet. *Sol. State Commun.* **152**, 1341–1349 (2012).
- Xia, F., Yan, H. & Avouris, P. The interaction of light and graphene: Basics, devices, and applications. *Proc. IEEE* **101**, 1717–1731 (2013).
- Xiao, D., Liu, G.-B., Feng, W., Xu, X. & Yao, W. Coupled spin and valley physics in monolayers of MoS₂ and other group-VI dichalcogenides. *Phys. Rev. Lett.* **108**, 196802 (2012).
- Zeng, H., Dai, J., Yao, W., Xiao, D. & Cui, X. Valley polarization in MoS₂ monolayers by optical pumping. *Nature Nanotech.* **7**, 490–493 (2012).
- Mak, K. F., He, K., Shan, J. & Heinz, T. F. Control of valley polarization in monolayer MoS₂ by optical helicity. *Nature Nanotech.* **7**, 494–498 (2012).
- Cao, T. *et al.* Valley-selective circular dichroism of monolayer molybdenum disulphide. *Nature Commun.* **3**, 887 (2012).
- Morita, A. Semiconducting black phosphorus. *Appl. Phys. A* **39**, 227–242 (1986).
- Tran, V., Soklaski, R., Liang, Y. & Yang, L. Layer-controlled band gap and anisotropic excitons in few-layer black phosphorus. *Phys. Rev. B* **89**, 235319 (2014).
- Lee, E. J. H., Balasubramanian, K., Weitz, R. T., Burghard, M. & Kern, K. Contact and edge effects in graphene devices. *Nature Nanotech.* **3**, 486–490 (2008).
- Xia, F. *et al.* Photocurrent imaging and efficient photon detection in a graphene transistor. *Nano Lett.* **9**, 1039–1044 (2009).
- Park, J., Ahn, Y. H. & Ruiz-Vargas, C. Imaging of photocurrent generation and collection in single-layer graphene. *Nano Lett.* **9**, 1742–1746 (2009).
- Xu, X., Gabor, N. M., Alden, J. S., van der Zande, A. M. & McEuen, P. L. Photo-thermoelectric effect at a graphene interface junction. *Nano Lett.* **10**, 562–566 (2009).
- Bistrizter, R. & MacDonald, A. H. Electronic cooling in graphene. *Phys. Rev. Lett.* **102**, 206410 (2009).
- Song, J. C. W., Rudner, M. S., Marcus, C. M. & Levitov, L. S. Hot carrier transport and photocurrent response in graphene. *Nano Lett.* **11**, 4688–4692 (2011).

41. George, P. A. *et al.* Ultrafast optical-pump terahertz-probe spectroscopy of the carrier relaxation and recombination dynamics in epitaxial graphene. *Nano Lett.* **8**, 4248–4251 (2008).
42. Sun, D. *et al.* Ultrafast relaxation of excited Dirac fermions in epitaxial graphene using optical differential transmission spectroscopy. *Phys. Rev. Lett.* **101**, 157402 (2008).
43. Kim, R., Perebeinos, V. & Avouris, P. Relaxation of optically excited carriers in graphene. *Phys. Rev. B* **84**, 075449 (2011).
44. Winzer, T., Knorr, A. & Malić, E. Carrier multiplication in graphene. *Nano Lett.* **10**, 4839–4843 (2010).
45. Tielrooij, K. J. *et al.* Photoexcitation cascade and multiple hot-carrier generation in graphene. *Nature Phys.* **9**, 248–252 (2013).
46. Gabor, N. M. *et al.* Hot carrier-assisted intrinsic photoresponse in graphene. *Science* **334**, 648–652 (2011).
47. Freitag, M., Low, T., Xia, F. & Avouris, P. Photoconductivity of biased graphene. *Nature Photon.* **7**, 53–59 (2013).
48. Shi, S.-F. *et al.* Controlling graphene ultrafast hot carrier response from metal-like to semiconductor-like by electrostatic gating. *Nano Lett.* **14**, 1578–1582 (2014).
49. Tan, Y.-W., Zhang, Y., Stormer, H. L. & Kim, P. Temperature dependent electron transport in graphene. *Eur. Phys. J. Spec. Top.* **148**, 15–18 (2007).
50. He, K., Poole, C., Mak, K. F. & Shan, J. Experimental demonstration of continuous electronic structure tuning via strain in atomically thin MoS₂. *Nano Lett.* **13**, 2931–2936 (2013).
51. Castellanos-Gomez, A. *et al.* Local strain engineering in atomically thin MoS₂. *Nano Lett.* **13**, 5361–5366 (2013).
52. Ramasubramaniam, A., Naveh, D. & Towe, E. Tunable band gaps in bilayer transition-metal dichalcogenides. *Phys. Rev. B* **84**, 205325 (2011).
53. Duerloo, K. N., Li, Y. & Reed, E. J. Structural phase transitions in two-dimensional Mo- and W-dichalcogenide monolayers. *Nature Commun.* **5**, 4214 (2014).
54. Zhang, Y. J., Oka, T., Suzuki, R., Ye, J. T. & Iwasa, Y. Electrically switchable chiral light-emitting transistor. *Science* **344**, 725–728 (2014).
55. Ross, J. S. *et al.* Electrically tunable excitonic light-emitting diodes based on monolayer WSe₂ p-n junctions. *Nature Nanotech.* **9**, 268–272 (2014).
56. Baugher, B. W. H., Churchill, H. O. H., Yang, Y. & Jarillo-Herrero, P. Optoelectronic devices based on electrically tunable p-n diodes in a monolayer dichalcogenides. *Nature Nanotech.* **9**, 262–267 (2014).
57. Pospischil, A., Furchi, M. & Mueller, T. Solar-energy conversion and light emission in an atomic monolayer p-n diode. *Nature Nanotech.* **9**, 257–261 (2014).
58. Jones, A. M. *et al.* Optical generation of excitonic valley coherence in monolayer WSe₂. *Nature Nanotech.* **8**, 634–638 (2013).
59. Zhang, C., Johnson, A., Hsu, C.-L., Li, L.-J. & Shih, C.-K. Direct imaging of band profile in single layer MoS₂ on graphite: Quasiparticle energy gap, metallic edge states and edge band bending. *Nano Lett.* **14**, 2243–2247 (2014).
60. Chernikov, A. *et al.* Exciton binding energy and non-hydrogenic Rydberg series in monolayer WS₂. *Phys. Rev. Lett.* **113**, 076802 (2014).
61. Mak, K. F. *et al.* Tightly bound trions in monolayer MoS₂. *Nature Mater.* **12**, 207–211 (2012).
62. Ross, J. S. *et al.* Electrical control of neutral and charged excitons in a monolayer semiconductor. *Nature Commun.* **4**, 1474 (2013).
63. Yu, H., Liu, G.-B., Gong, P., Xu, X. & Yao, W. Dirac cones and Dirac saddle points of bright excitons in monolayer transition metal dichalcogenides. *Nature Commun.* **5**, 3876 (2014).
64. Britnell, L. *et al.* Strong light-matter interactions in heterostructures of atomically thin films. *Science* **340**, 1311–1314 (2013).
65. Fortin, E. & Sears, W. M. Photovoltaic effect and optical absorption in MoS₂. *J. Phys. Chem. Solids* **43**, 881–884 (1982).
66. Yu, W. J. *et al.* Highly efficient gate-tunable photocurrent generation in vertical heterostructures of layered materials. *Nature Nanotech.* **8**, 952–958 (2013).
67. Konstantatos, G. *et al.* Hybrid graphene-quantum dot phototransistors with ultrahigh gain. *Nature Nanotech.* **7**, 363–368 (2012).
68. Roy, K. *et al.* Graphene-MoS₂ hybrid structures for multifunctional photoresponsive memory devices. *Nature Nanotech.* **8**, 826–830 (2013).
69. Maier, S. *Plasmonics: Fundamentals and Applications* 1st edn (Springer, 2007).
70. Wunsch, B., Stauber, T. & Guinea, F. Dynamical polarization of graphene at finite doping. *New J. Phys.* **8**, 318 (2006).
71. Hwang, E. H. & Das Sarma, S. Dielectric function, screening, and plasmons in two-dimensional graphene. *Phys. Rev. B* **75**, 205418 (2007).
72. Abedinpour, S. *et al.* Drude weight, plasmon dispersion, and ac conductivity in doped graphene sheets. *Phys. Rev. B* **84**, 045429 (2011).
73. Thongrattanasiri, S., Manjavacas, A. & Garcia de Abajo, F. J. Quantum finite-size effects in graphene plasmons. *ACS Nano* **6**, 1766–1775 (2012).
74. Jablan, M., Buljan, H. & Soljačić, M. Plasmonics in graphene at infrared frequencies. *Phys. Rev. B* **80**, 245435 (2009).
75. Koppens, F. H. L., Chang, D. E. & Garcia de Abajo, F. J. Graphene plasmonics: a platform for strong light-matter interactions. *Nano Lett.* **11**, 3370–3377 (2011).
76. Ju, L. *et al.* Graphene plasmonics for tunable terahertz metamaterials. *Nature Nanotech.* **6**, 630–634 (2011).
77. Yan, H. *et al.* Tunable infrared plasmonic devices using graphene/insulator stacks. *Nature Nanotech.* **7**, 330–334 (2012).
78. Fei, Z. *et al.* Infrared nanoscopy of Dirac plasmons at the graphene-SiO₂ interface. *Nano Lett.* **11**, 4701–4705 (2011).
79. Fei, Z. *et al.* Gate-tuning of graphene plasmons revealed by infrared nano-imaging. *Nature* **487**, 82–85 (2012).
80. Chen, J. *et al.* Optical nano-imaging of gate-tunable graphene plasmons. *Nature* **487**, 77–81 (2012).
81. Yan, H. *et al.* Damping pathways of mid-infrared plasmons in graphene nanostructures. *Nature Photon.* **7**, 394–399 (2013).
82. Brar, V. W., Jang, M. S., Sherrott, M., Lopez, J. J. & Atwater, H. A. Highly confined tunable mid-infrared plasmonics in graphene nanoresonators. *Nano Lett.* **13**, 2541–2547 (2013).
83. Dai, S. *et al.* Tunable phonon polaritons in atomically thin van der Waals crystals of boron nitride. *Science* **343**, 1125–1129 (2014).
84. Liu, Y. & Willis, R. F. Plasmon-phonon strongly coupled mode in epitaxial graphene. *Phys. Rev. B* **81**, 081406 (2010).
85. Brar, V. W. *et al.* Hybrid surface-phonon-plasmon polariton modes in graphene/monolayer h-BN heterostructures. *Nano Lett.* **14**, 3876–3880 (2014).
86. Li, L. *et al.* Black phosphorus field-effect transistors. *Nature Nanotech.* **9**, 372–377 (2014).
87. Liu, H. *et al.* Phosphorene: An unexplored 2D semiconductor with a high hole mobility. *ACS Nano* **8**, 4033–4041 (2014).
88. Buscema, M. *et al.* Fast and broadband photoresponse of few-layer black phosphorus field-effect transistors. *Nano Lett.* **14**, 3347–3352 (2014).
89. Xia, F., Wang, H. & Jia, Y. Rediscovering black phosphorus as an anisotropic layered material for optoelectronics and electronics. *Nature Commun.* **5**, 4458 (2014).
90. Koenig, S., Doganov, R., Schmidt, H., Castro Neto, A. & Ozilimaz, B. Electric field effect in ultrathin black phosphorus. *Appl. Phys. Lett.* **104**, 103106 (2014).
91. Rodin, A. S., Carvalho, A. & Castro Neto, A. H. Strain-induced gap modification in black phosphorus. *Phys. Rev. Lett.* **112**, 176801 (2014).
92. Qiao, J., Kong, X., Hu, Z., Yang, F. & Ji, W. High-mobility transport anisotropy and linear dichroism in few-layer black phosphorus. *Nature Commun.* **5**, 4475 (2014).
93. Low, T. *et al.* Tunable optical properties of multilayers black phosphorus thin films. *Phys. Rev. B* **90**, 075434 (2014).
94. Low, T. *et al.* Plasmons and screening in monolayer and multilayer black phosphorus. *Phys. Rev. Lett.* **113**, 106802 (2014).
95. Fei, R. *et al.* Enhanced thermoelectric efficiency via orthogonal electrical and thermal conductances in phosphorene. *Nano Lett.* <http://doi.org/wxz> (2014).
96. Yu, L. *et al.* Graphene/MoS₂ hybrid technology for large-scale two-dimensional electronics. *Nano Lett.* **14**, 3055–3063 (2014).
97. Osters, O. *et al.* Synthesis and identification of metastable compounds: Black arsenic — science or fiction? *Angew. Chemie* **51**, 2994–2997 (2012).

Acknowledgements

We thank X. Xu at the University of Washington, Seattle and M. Dresselhaus at Massachusetts Institute of Technology for insightful comments. We would also like to thank T. Low at the University of Minnesota for his input at the early stage of this project and L. Wang at the University of Southern California for designing Fig. 6c,d. F.X. acknowledges support from the Office of Naval Research (N00014-14-1-0565), the Air Force Office of Scientific Research (FA9550-14-1-0277) and the National Science Foundation (CRISP NSF MRSEC DMR-1119826). H.W. acknowledges support from the Army Research Laboratory (W911NF-14-2-0113). D.X. acknowledges support from the Department of Energy (SC0012509), the Air Force Office of Scientific Research (FA9550-14-1-0277), and the National Science Foundation (EFRI-1433496).

Author contributions

F.X. and H.W. led the project. All authors contributed significantly to the preparation of the manuscript.

Additional information

Reprints and permissions information is available online at www.nature.com/reprints. Correspondence and requests for materials should be addressed to F.X.

Competing financial interests

The authors declare no competing financial interests.